Received: 15 March 2022 | Revised: 28 February 2023 | Accepted: 20 March 2023

DOI: 10.1002/rnc.6697

RESEARCH ARTICLE

WILEY

Nonlinear model predictive control for autonomous vehicle drifting

Zhuqing Shi[1,2] | **Hong Chen**[2,3] | **Shuyou Yu**[1,2] | **Rolf Findeisen**[4] | **Hongyan Guo**[1,2]

[1]State Key Laboratory of Automotive Simulation and Control, Jilin University, Changchun, China

[2]Department of Control Science and Engineering, Jilin University, Changchun, China

[3]College of Electronics and Information Engineering, Tongji University, Shanghai, China

[4]Control and Cyber-Physical Systems Laboratory, Technical University of Darmstadt, Darmstadt, Germany

Correspondence
Shuyou Yu, Department of Control Science and Engineering, Jilin University, Changchun, 130025, China.
Email: shuyou@jlu.edu.cn

Funding information
National Natural Science Foundation of China, Grant/Award Numbers: 61790564, U1964202, U19A2069; Natural Science Foundation of Jilin Province, Grant/Award Number: YDZJ202101ZYTS169

Abstract

In this paper, nonlinear model predictive control (NMPC) is proposed for autonomous vehicle drifting, that is, stabilizing the vehicle at a desired unstable equilibrium point. Firstly, a three-degree-of-freedom vehicle model with a nonlinear tire model is introduced, and the equilibrium points are calculated. The relationship between the desired unstable equilibrium point and the lateral stability region is analyzed based on the phase plane method. Secondly, NMPC is designed to force vehicle states to stay around the desired unstable equilibrium point, that is, to keep the vehicle in sustained drifting. The terminal region and terminal constraint of NMPC are determined off-line to guarantee stability. Thirdly, Koopman operator theory and dynamic mode decomposition with control are introduced to obtain an approximately linear model, by which the nonlinear optimization problem is converted to a quadratic programming problem. Finally, comparative experiments are conducted by simulation, in which various model uncertainties are considered. The effectiveness of the proposed approach to achieve sustained autonomous drifting and to ensure vehicle safety is illustrated, and the efficient implementation of the proposed approach is also shown.

KEYWORDS

Koopman operator, model predictive control, sustained drifting, terminal constraint

1 | INTRODUCTION

Vehicle safety is a key issue in autonomous driving.[1] As an essential factor affecting vehicle safety, vehicle handling stability quickly deteriorates under challenging scenarios, such as sharp cornering at high speed.[2] For example, a possibly recurrent chaotic motion will lead to severe skidding and rollover,[3] which is a serious threat to vehicle safety, should be avoided.[4] Thus, the study of stabilizing a vehicle beyond its handling limits is necessary for autonomous driving.

The severe deterioration of vehicle handling stability will lead to the vehicle losing control, that is, the vehicle states can not converge to a stable point.[5] To address this issue, conventional research on vehicle dynamics has studied the vehicle stability region, for example, Inagaki et al.[6] approximate the stability region using the phase plane method. Within the stability region, vehicle trajectories that start from different initial points converge to a stable equilibrium point. Outside the stability region, the vehicle state deviates from all equilibrium points (including two unstable equilibrium points). By restricting vehicle states inside the stability region, Inagaki et al.[7] propose the scheme of vehicle stability control (VSC), which is introduced to the market by Toyota.[8] Similar technology is developed as well with different names, such as the electronic stability program (ESP).[9]

Unlike VSC or ESP, drift control forces vehicle states out of the stability region, such as the large yaw rate and sideslip angle, to accomplish sharp cornering at high speed. Some studies have designed the combination method of closed-loop and open-loop control based on racers' experience to achieve vehicle drift.[10] Kolter et al.[11] present a probabilistic approach to combine open-loop and closed-loop control for a vehicle drifting into a parking spot. The open-loop control is designed for initiating vehicle states to temporarily drift along a predefined ideal trajectory, that is, transient drifting. Zhang et al.[12] propose a hybrid open-loop and closed-loop control strategy to achieve transient drifting along the turning trajectory. The open-loop maneuvers are designed by observing expert drivers' operation, and the closed-loop part is designed by a linear quadratic regulator (LQR) approach. However, it is verified that the controller relies on the open-loop control instead of LQR when the tracking error is significant. For open-loop control, the disadvantage of poor resistance to disturbances is inevitable.

In addition to transient drifting, researchers have widely investigated sustained drifting. Voser et al.[13] present the existence of unstable "drift equilibria" related to steady state cornering with a large sideslip angle, where the directions of cornering and steering wheel are opposite, namely countersteer configuration. Based on the linearization of a bicycle model with nonlinear tire characteristics, the separate proportional speed controller and state feedback steering controller are designed to stabilize vehicle states at the equilibrium point, which is proven to achieve autonomous drift in the testbed. Inspired by this work, Hindiyeh et al.[14] incorporate longitudinal dynamics in the bicycle model, that is, a 3-degree-of-freedom (3-DOF) bicycle model. They reveal the steady state cornering conditions associated with sustained drifting at the drift equilibria, that is, the execution of large sideslip angle, rear tire lateral force saturation, and countersteer. Pole placement and proportional gain are independently designed to control steering and vehicle speed, respectively, which maintains vehicle states at the desired drift equilibrium. In the research above, sequences of open-loop control are retained to guide vehicle states into the neighborhood of the desired drift equilibrium.

Recently, various control methods have been applied in vehicle drift control, such as LQR,[15] robust control,[16] sliding mode control,[17] dynamic surface control technique,[18] and backstepping control.[19] Model predictive control (MPC), which is capable of explicitly dealing with state and input constraints, is also used for achieving autonomous drifting. Kuck[20] evaluates the performance of MPC in remote control of sustained drift. Based on the linearization of a bicycle model with a nonlinear Fiala tire model, linear MPC is designed to stabilize vehicle states at the unstable equilibrium point. Manuel et al.[21] present an approach to teach a vehicle to drift like a professional driver, which is employed by a hybrid structure consisting of an MPC and feedforward Neural Networks (NNs). A lower-level MPC stabilizes the vehicle around the equilibrium states, and feedforward NNs provide the upper-level drift references and tire parameters. Guo et al.[22] and Hu et al.[23] use the local linearization method to obtain a linear vehicle dynamics model at the unstable equilibrium point, and design MPC to achieve sustained drift. For efficient computation of MPC, the control inputs are updated by solving the quadratic programming (QP) problem at each time instant. However, the system stability is not considered in MPC design.

Since the computational burden of MPC will increase with the complexity of system dynamics, researchers use Taylor expansion to obtain its linearized model of systems at the equilibrium point. Such a linearized model is only valid near the equilibrium point, and the Jacobian matrix must be solved at each instant according to variant equilibrium points.[24] Such weakness can be avoided by global linearization methods, for example, Koopman operator theory.[25] Koopman operator theory uses an infinite dimensional linear model to describe the complex nonlinear system, which can retain primarily the nonlinear dynamics of the system. Korda et al.[26] and Zhang et al.[27] have applied Koopman operator theory in MPC for the prediction model. Due to the implementation difficulty of the infinite dimensional Koopman operator, dynamic mode decomposition with control (DMDc) is developed to approximate the Koopman operator in finite dimensions.[28] DMDc makes it possible to obtain a linear model with control for the design of MPC.[29]

This paper proposes a quasi-infinite horizon nonlinear model predictive control (NMPC) approach for sustained drifting. A nonlinear 3-DOF vehicle model with nonlinear tire dynamics is adopted, where the influence of air resistance is considered. Based on the 3-DOF vehicle model, the desired unstable equilibrium point is calculated, and the lateral stability region is estimated using the phase plane method. The control objective is to drive vehicle states outside the stability region to the desired unstable equilibrium point. NMPC is designed for sustained drifting, where the terminal region and the terminal constraint are calculated off-line to guarantee stability. To efficiently implement the proposed approach, Koopman operator theory and DMDc are taken to approximately obtain a linearized vehicle model. The computational burden is primarily reduced by converting the nonlinear optimization problem to a QP problem. Comparative simulations that include system uncertainties are carried out to illustrate the effectiveness of the proposed approaches.

This paper is organized as follows: Section 2 presents the control problem based on a 3-DOF vehicle system model and the vehicle dynamics analysis in the phase plane, Section 3 designs an NMPC with guaranteed stability which forces vehicle states to stay at the desired equilibrium point and provides an approach for efficiently implementing autonomous drifting, Section 4 illustrates the effectiveness and priority of the proposed approach by comparative experiments, Section 5 is the conclusion including future work.

2 | PROBLEM STATEMENT

In this section, a 3-DOF vehicle system model with nonlinear tire dynamics is introduced, and the influence of air resistance is considered in vehicle drifting. Then different dynamic characteristics of vehicle states are analyzed around stable and unstable equilibrium points in the phase plane. Finally, the control objective is proposed, that is, stabilizing vehicle states outside the stability region to the desired unstable equilibrium point.

2.1 | Vehicle system model

A 3-DOF (lateral velocity, yaw rate, and longitudinal velocity) vehicle model is introduced to describe nonlinear dynamics of vehicle drifting.[30] Since vehicle drifting typically occurs at high speed and sharp cornering, the 3-DOF vehicle model is adopted instead of the 2-DOF vehicle bicycle model to consider the changing longitudinal velocity. As the schematic diagram of the 3-DOF vehicle model shown in Figure 1, the left and right tires are lumped into one tire, which is consistent with the assumption of the 2-DOF vehicle bicycle model. The equations of 3-DOF vehicle model are:[30]

$$\begin{cases} \dot{v}_y = \frac{1}{m}\left(F_{yf}\cos\delta_f + F_{yr} - C_y A_{air}\frac{\rho}{2}v^2\right) - v_x\gamma, \\ \dot{\gamma} = \frac{1}{I_z}\left(F_{yf}l_f\cos\delta_f - F_{yr}l_r\right), \\ \dot{v}_x = \frac{1}{m}\left(F_{xr} - F_{yf}\sin\delta_f - C_x A_{air}\frac{\rho}{2}v^2\right) + v_y\gamma, \end{cases} \tag{1}$$

where v_y, γ, and v_x are lateral velocity, yaw rate, and longitudinal velocity, respectively, F_{xr} is the longitudinal force of rear tire, F_{yf} and F_{yr} are lateral forces of the front tire and rear tire, respectively. The influence of air resistance on lateral and longitudinal velocity is considered in vehicle dynamics, where C_y and C_x are lateral and longitudinal air resistance coefficients, respectively, A_{air} is the frontal area of driving direction, and ρ is air density. As shown in Figure 1, the direction of vehicle velocity v $(v^2 = v_x^2 + v_y^2)$ is the vehicle heading direction, the sideslip angle $\beta = \arctan(v_y/v_x)$ is the angle between v_x and v, δ_f is front wheel steering angle, m is vehicle mass, I_z is the moment of inertia, l_f and l_r are the distances from the center of mass (c.m.) to the front and rear axes, respectively.

In (1), the lateral forces of the front tire and rear tire are represented by Magic Formula,[31] that is,

$$F_{yf} = D_{sf}\sin(C_{sf}\arctan(B_{sf}\alpha_f)), \tag{2a}$$

$$F_{yr} = D_{sr}\sin(C_{sr}\arctan(B_{sr}\alpha_r)), \tag{2b}$$

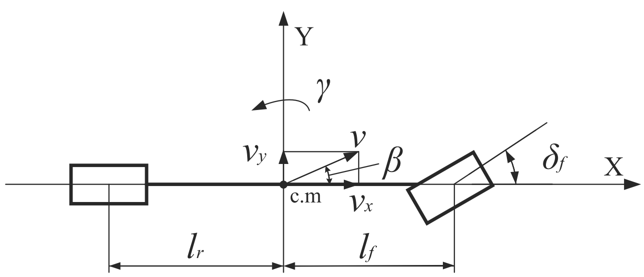

FIGURE 1 Schematic diagram of 3-DOF vehicle model.

TABLE 1 Parameters of the vehicle system.

Parameters	Values	Parameters	Values
Vehicle mass m /(kg)	1833	Distance from c.m. to front axes l_f /(m)	1.4
Moment of inertia I_z / (kg $\cdot$ m^2)	3065	Distance from c.m. to rear axes l_r /(m)	1.65
Road friction coefficient $\mu/(\cdot)$	0.75	Gravity acceleration g / (m/s^2)	9.81
Front/rear tire coefficient B_{sf} / B_{sr}	11.16/11.37	Air frontal area A_{air} /(m^2)	1.8
Front/rear tire coefficient C_{sf} / C_{sr}	1.68/1.75	Air density ρ / (kg/m^3)	1.206
Front/rear tire coefficient D_{sf} / D_{sr}	−7295.9/ − 6190.4	Air resistance coefficient C_y / C_x	−0.35/0.37

where B_{sf}, C_{sf}, and D_{sf} are front tire coefficients, B_{sr}, C_{sr}, and D_{sr} are rear tire coefficients, α_f and α_r are sideslip angle of front tire and rear tire, respectively, which can be approximately calculated as:[31]

$$\alpha_f \approx \arctan\left(\frac{v_y + l_f\gamma}{v_x}\right) - \delta_f, \tag{3a}$$

$$\alpha_r \approx \arctan\left(\frac{v_y - l_r\gamma}{v_x}\right). \tag{3b}$$

Since the tire force should be lower than the ground adhesion,[31] the forces of the front and rear tires should satisfy the constraints as follows:[12]

$$|F_{yf}| \leq \mu F_{zf}, \tag{4a}$$

$$|F_{xr}| \leq \mu F_{zr}, \tag{4b}$$

$$\sqrt{F_{xr}^2 + F_{yr}^2} \leq \mu F_{zr}, \tag{4c}$$

where μ is the road friction coefficient, F_{zf} and F_{zr} are the vertical load of front and rear tires, respectively. Suppose F_{yf} is given, then δ_f can be obtained by solving the inverse function of (2a) and (3a), that is,

$$\alpha_f = \begin{cases} \tan(\arcsin(-F_{yf}/\mu F_{zf})/C_{sf})/B_{sf}, & \text{if } |F_{yf}| < \mu F_{zf}, \\ \tan\left(-\frac{2\pi}{C_{sf}}\right)/B_{sf} \cdot \operatorname{sgn}(F_{yf}), & \text{if } |F_{yf}| \geq \mu F_{zf}, \end{cases} \tag{5a}$$

$$\delta_f = \arctan\left(\frac{v_y + l_f\gamma}{v_x}\right) - \alpha_f. \tag{5b}$$

The parameters are taken from an E-class Sedan car with 215/70 R17 tires in vehicle dynamic software CarSim, which are listed in Table 1. The tire coefficients are identified based on the Levenberg-Marquardt method,[32] which uses data of the actual tire force on the dry concrete road surface. The corresponding road friction coefficient is set as $\mu = 0.75$. The air resistance coefficients are functions of the aerodynamic side slip angle β_{air}, which is approximately set to $\beta_{air} = -10°$ (here the symbol ° is the unit of angle in degree). Note that uncertainties of road friction and air resistance coefficients are considered in the simulation of Section 4.

2.2 | Phase plane analysis

Rewrite (1) into a general form of nonlinear system, namely the original system:

$$\dot{x} = F(x, u), \tag{6}$$

where $x = [v_y \;\; \gamma \;\; v_x]^{\mathrm{T}}$ and $u = [F_{yf} \;\; F_{xr}]^{\mathrm{T}}$ are the system state and the control input, respectively. An equilibrium point $x = x^{eq}$ of a nonlinear system has the property that whenever the state of the system starts at x^{eq}, it will remain at x^{eq} for all future time.[33] For system (6), the equilibrium point (x^{eq}, u^{eq}) is the root of the equation:

$$F(x, u) = 0, \tag{7}$$

where $x^{eq} = \left[v_y^{eq} \;\; \gamma^{eq} \;\; v_x^{eq}\right]^{\mathrm{T}}$ and $u^{eq} = \left[F_{yf}^{eq} \;\; F_{xr}^{eq}\right]^{\mathrm{T}}$ are the system state and control input, respectively, the symbol ϑ^{eq} represents the value of variable ϑ at the equilibrium point. Since there are five unknown variables (v_y^{eq}, γ^{eq}, v_x^{eq}, F_{yf}^{eq} and F_{xr}^{eq}) in (7), the variables δ_f^{eq} (corresponding to F_{yf}^{eq} by (5)) and v_x^{eq} are set in advance to solve the equilibrium points.

The results of x^{eq} with $\delta_f^{eq} \in [-8, 8]$ (°) are shown in Figure 2, the longitudinal velocity is $v_x^{eq} = 20$m/s and the interval is $\delta_f^{eq} = 1°$. Figure 2A,B represent the values of γ^{eq} and v_y^{eq}, respectively. As shown in Figure 2, there are three equilibrium points corresponding to each $\delta_f^{eq} \in [-3, 3]$ (°), which are represented by a red circle, a blue square, and a black square. Otherwise, there is only one equilibrium point indicated by a blue square or a black square.

The characteristic of these equilibrium points and the qualitative system behaviors near them can be determined via linearization concerning the point,[33] that is,

$$\dot{x}_l = A_l x_l + B_l u_l, \tag{8}$$

where $x_l = x - x^{eq}$, $u_l = u - u^{eq}$, and the matrix coefficients are as follows:

$$A_l = \left.\frac{\partial F}{\partial x}\right|_{x=x^{eq}, u=u^{eq}}, \quad B_l = \left.\frac{\partial F}{\partial u}\right|_{x=x^{eq}, u=u^{eq}}, \tag{9}$$

where the eigenvalues of A_l can be used to obtain the dynamics near equilibrium points.

Take the cases of $\delta_f^{eq} = 0°$, $\delta_f^{eq} = 2°$, and $\delta_f^{eq} = -10°$ as the representatives to intuitively illustrate the characteristics results in the phase plane. The state trajectories derived by numerical integration of (6) are shown in lateral velocity-yaw rate (v_y - γ) phase plane (cf. Figure 3), where gray lines represent the state trajectories starting from the initial states shown in black dots. Based on the state trajectories and phase plane method,[6,34] the stability regions are estimated and shown by red shaded areas in Figure 3A,B. The stability region is the indicator of vehicle stability during critical maneuvers, that is, the vehicle state inside the stability region will move to the stable equilibrium point (shown in red circle) along a specific trajectory.[35] Otherwise, the vehicle state will not converge to a equilibrium point. That is, the vehicle will lose lateral stability without external control.

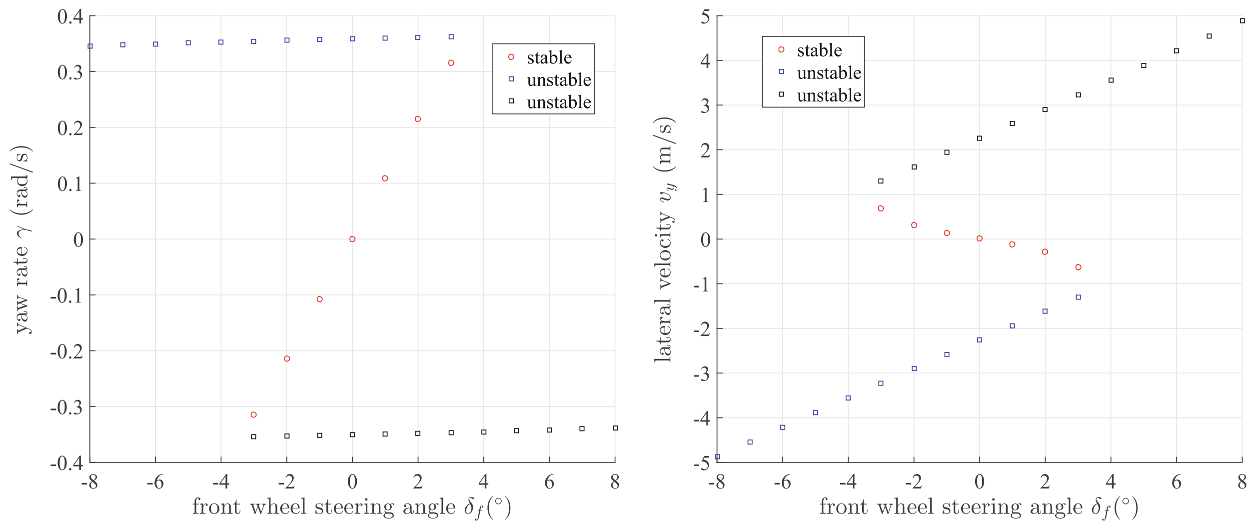

(A) Yaw rate γ^{eq} (B) Lateral velocity v_y^{eq}

FIGURE 2 Equilibrium points with $v_x^{eq} = 20$m/s.

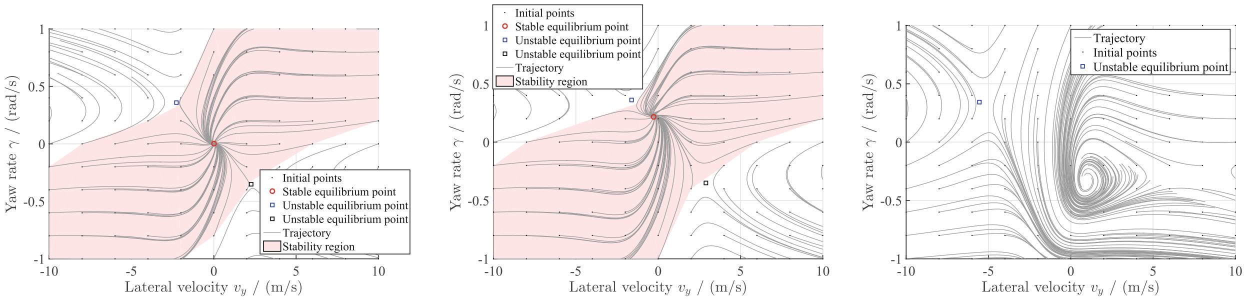

(A) $\delta_f^{eq} = 0°$ (B) $\delta_f^{eq} = 2°$ (C) $\delta_f^{eq} = -10°$

FIGURE 3 Lateral velocity-yaw rate phase plane.

When entering a sharp corner at high speed, the vehicle state easily exceeds its stability region, which seriously threatens vehicle safety.[36] For example, the vehicle state from the black dot bypasses the unstable equilibrium points (represented by a blue square and a black square in Figure 3A,B) but does not converge. Even worse, the chaotic motion may occur around unstable equilibrium points.[37] It is worth noting that if δ_f is large enough, the static bifurcation will appear, which leads to the disappearance of both the stability region and the stable equilibrium point.[35] As shown in Figure 3C, only an unstable equilibrium point is left. For this circumstance, conventional methods that restrict vehicle states inside the stability region are inappropriate for stabilizing vehicles.

2.3 | Control objective

This paper mainly studies an NMPC approach of steady state drifting to stabilize the vehicle state outside the stability region, which avoids serious accidents even under high speed and sharp cornering operating conditions. The control objective of NMPC is to achieve sustained drifting by tracking the unstable equilibrium point, that is, forcing vehicle states to converge to x^{ref}:

$$\lim_{k\to\infty} \|x(k) - x^{ref}(k)\| = 0, \tag{10}$$

where k is time instant, (x^{ref}, u^{ref}) is the desired unstable equilibrium point, $x^{ref} = \begin{bmatrix} v_y^{ref} & \gamma^{ref} & v_x^{ref} \end{bmatrix}^{\mathrm{T}}$ and $u^{ref} = \begin{bmatrix} F_{yf}^{ref} & F_{xr}^{ref} \end{bmatrix}^{\mathrm{T}}$ satisfy (7). The symbol ζ^{ref} represents the value of variable ζ at the desired unstable equilibrium point.

Remark 1. The sustained drifting is the concern of this paper, while the transient drifting along a certain trajectory will be introduced in the future.

3 | NMPC DESIGN FOR AUTONOMOUS DRIFTING

In this section, a quasi-infinite horizon NMPC is designed,[38] which takes the terminal constraint and the terminal penalty into account. Considering the real-time implementation of autonomous drifting, an efficient implementation is proposed.

The discrete-time system to be controlled is obtained from the original system (6) using the Runge-Kutta method with the sampling time $T_s = 0.01$s, namely the controlled system:

$$x(k+1) = F(x(k), u(k)), \tag{11}$$

where $u(k) \in U$ and $x(k) \in X$ are the system state and control input at the time instant $k \in \mathbb{Z}_+$ ($\mathbb{Z}_+$ is positive integer), respectively. The constraints are

$$U = \{u \in \mathbb{R}^2 \mid -7295.9 \le F_{yf} \le 7295.9, \quad -6190.4 \le F_{xr} \le 6190.4\}, \tag{12a}$$

$$X = \{x \in \mathbb{R}^3 \mid -20 \le v_y \le 20, \quad -1 \le \gamma \le 1, \quad 0 \le v_x \le 40\}, \tag{12b}$$

where the control constraint U is calculated by (4a) and (4b), the unit of F_{yf} and F_{xr} is Newton (N). In the state constraint set X, the ranges of v_y(m/s) and γ(rad/s) are determined from the feasible values of lateral velocity and yaw rate in actual scenarios,[39] the range of v_x(m/s) indicates that the vehicle moves forward reasonably.

For sake of controller design, transform the equilibrium point of the original system (6) from (x^{ref}, u^{ref}) to $(\mathbf{0}, \mathbf{0})$ by coordinate transformation:

$$\Delta x = x - x^{ref}, \quad \Delta u = u - u^{ref}, \tag{13}$$

where $\Delta x = [\Delta v_y \;\; \Delta\gamma \;\; \Delta v_x]^{\mathrm{T}} = [v_y - v_y^{ref} \;\; \gamma - \gamma^{ref} \;\; v_x - v_x^{ref}]^{\mathrm{T}}$ and $\Delta u = [\Delta F_{yf} \;\; \Delta F_{xr}]^{\mathrm{T}} = [F_{yf} - F_{yf}^{ref} \;\; F_{xr} - F_{xr}^{ref}]^{\mathrm{T}}$. Then the original system is converted to:

$$\Delta\dot{x} = \tilde{F}(\Delta x, \Delta u), \tag{14}$$

where Δx and Δu satisfy the equation $\tilde{F}(\mathbf{0}, \mathbf{0}) = \mathbf{0}$.

Then the transformed system is obtained by discretizing (14) with T_s:

$$\Delta x(k+1) = \tilde{f}(\Delta x(k), \Delta u(k)), \tag{15}$$

where $\Delta x(k) \in \mathbb{R}^3$ and $\Delta u(k) \in \mathbb{R}^2$ are the system state and control input at the time instant $k \in \mathbb{Z}_+$, respectively. The initial state is $\Delta x(0) = \Delta x_0$. For all $k \geq 0$, the system state and control input satisfy:

$$\Delta x(k) \in \Delta X, \quad \Delta u(k) \in \Delta U, \tag{16}$$

where ΔX and ΔU denote the feasible sets of system state and control input for the discrete-time transformed system (15), respectively, which can be obtained by (12) and (13), that is,

$$\Delta U = \left\{ \Delta u \in \mathbb{R}^2 \mid -7295.9 - F_{yf}^{ref} \leq \Delta F_{yf} \leq 7295.9 - F_{yf}^{ref}, \;\; -6190.4 - F_{xr}^{ref} \leq \Delta F_{xr} \leq 6190.4 - F_{xr}^{ref} \right\}, \tag{17a}$$

$$\Delta X = \left\{ \Delta x \in \mathbb{R}^3 \mid -20 - v_y^{ref} \leq \Delta v_y \leq 20 - v_y^{ref}, \;\; -1 - \gamma^{ref} \leq \Delta\gamma \leq 1 - \gamma^{ref}, \;\; -v_x^{ref} \leq \Delta v_x \leq 40 - v_x^{ref} \right\}. \tag{17b}$$

3.1 | NMPC with guaranteed stability

In this subsection, it is assumed that the states are completely obtained. Neither external disturbance nor the model perturbation is considered.[40] The uncertainties of controlled system are considered in numerical simulation.

The transformed system (15) satisfies the requirements as follows:

(A1) $\tilde{f} : \mathbb{R}^3 \times \mathbb{R}^2 \to \mathbb{R}^3$ is continuous, and $\tilde{f}(\mathbf{0}, \mathbf{0}) = \mathbf{0}$, that is, $(\mathbf{0}, \mathbf{0})$ is an equilibrium of the system.
(A2) $\Delta U \in \mathbb{R}^2$ is compact and convex, $\Delta X \in \mathbb{R}^3$ is connected, the point $(\mathbf{0}, \mathbf{0})$ is contained in the interior of $\Delta X \times \Delta U$.

Then the open-loop optimization problem of quasi-infinite horizon NMPC at the time instant k is formulated as

Problem 1.

$$\underset{\Delta\bar{u}(\cdot)}{minimize} \quad J(\Delta x(k), \Delta\bar{u}(\cdot)) \tag{18a}$$

$$\text{subject to} \quad \Delta\bar{x}(\tau+1|k) = \tilde{f}(\Delta\bar{x}(\tau|k), \Delta\bar{u}(\tau|k)), \tag{18b}$$

$$\Delta\bar{x}(k|k) = \Delta x(k), \tag{18c}$$

$$\Delta\bar{u}(\tau|k) \in \Delta U, \quad \tau \in [k, k+N-1], \tag{18d}$$

$$\Delta\bar{x}(\tau|k) \in \Delta X, \quad \tau \in [k, k+N-1], \tag{18e}$$

$$\Delta\bar{x}(k+N|k) \in \Omega, \tag{18f}$$

where $\Delta\bar{x}(\tau|k)$ is the predicted state trajectory of the system starting from $\Delta x(k)$ under control input $\Delta\bar{u}(\cdot)$, N is the finite prediction horizon, ΔU and ΔX represent the constraints of control input and system state, respectively. The cost function is

$$J(\Delta x(k), \Delta\bar{u}(\cdot)) = \sum_{i=0}^{N-1} L(\Delta\bar{x}(k+i|k), \Delta\bar{u}(k+i|k)) + E(\Delta\bar{x}(k+N|k)) \tag{19a}$$

with

$$L(\Delta\bar{x}(k+i|k), \Delta\bar{u}(k+i|k)) = \Delta\bar{x}^{\mathrm{T}}(k+i|k)Q\Delta\bar{x}(k+i|k) + \Delta\bar{u}^{\mathrm{T}}(k+i|k))R\Delta\bar{u}(k+i|k)), \tag{19b}$$

$$E(\Delta\bar{x}(k+N|k)) = \Delta\bar{x}^{\mathrm{T}}(k+N|k)P\Delta\bar{x}(k+N|k), \tag{19c}$$

where the weighting matrices $Q \in \mathbb{R}^{3\times 3}$ and $R \in \mathbb{R}^{2\times 2}$ are positive definite and symmetric, and P is the weighting matrix of terminal penalty. The terminal set Ω and the terminal cost function $E(\Delta\bar{x}(k+N|k))$ will be illustrated in more detail later.

The problem of stabilizing a vehicle around an unstable equilibrium point is equivalent to finding a feasible solution to Problem 1. Suppose that the optimal solution of Problem 1 at the time instant k is

$$\mathbf{U}^*(k) = \{\Delta\bar{u}^*(k|k), \Delta\bar{u}^*(k+1|k), \dots, \Delta\bar{u}^*(k+N-1|k)\}, \tag{20}$$

where $\Delta u^*(k) := \Delta\bar{u}^*(k|k)$ is the actual control input. At next time instant $(k+1)$, the process above will be repeated with the measurement of state $\Delta x(k+1)$.

To guarantee the stability of the system (15) under control, terminal ingredients that include terminal constraints and terminal penalty are designed, where LQR is taken for the terminal control. Note that the terminal control law does not act on the vehicle.

The Jacobian linearization function of system (15) at the equilibrium point $(\mathbf{0}, \mathbf{0})$ is used to solve the controller, that is,

$$\Delta x(k+1) = \hat{A}\Delta x(k) + \hat{B}\Delta u(k), \tag{21}$$

with

$$\hat{A} = \left.\frac{\partial\tilde{f}}{\partial\Delta x}\right|_{(\mathbf{0},\mathbf{0})}, \quad \hat{B} = \left.\frac{\partial\tilde{f}}{\partial\Delta u}\right|_{(\mathbf{0},\mathbf{0})}. \tag{22}$$

Since there is an eigenvalue of matrix $\hat{A}$ out of the unit circle, the system (21) is open-loop unstable. The matrix $[\hat{B}\ \ \hat{A}\hat{B}\ \ \hat{A}^2\hat{B}]$ is row full rank, that is, system (21) is controllable and therefore stabilizable. Thus, there exists a linear state feedback control law $\Delta u = K\Delta x$ such that $A_k := \hat{A} + \hat{B}K$ is asymptotically stable. Define $Q^* = Q + K^{\mathrm{T}}RK \in \mathbb{R}^{3\times 3}$, and $\kappa > 1$ is constant, then the terminal ingredients satisfy:[38,41]

(C1) The discrete Lyapunov equation

$$A_k^{\mathrm{T}}PA_k - P + \kappa Q^* = 0 \tag{23}$$

can be calculated to obtain a unique symmetric positive-definite solution.

(C2) There exists a constant $\alpha \in (0, \infty)$ such that a neighborhood of equilibrium

$$\Omega := \left\{\Delta x(k) \in \Delta X | \Delta x^{\mathrm{T}}(k)P\Delta x(k) \le \alpha\right\} \tag{24}$$

is the terminal region of system (15). The corresponding terminal controller and terminal penalty function are $\Delta u = K\Delta x$ and $\Delta x^{\mathrm{T}}(k)P\Delta x$, respectively. While Problem 1 is feasible at the initial instant, recursive feasibility of Problem 1 and the stability of vehicle around the desired unstable equilibrium point are guaranteed.

Remark 2. Although robust MPC framework can handle uncertainties, it is conservative and computationally heavy in general. Instead, previous studies have revealed that MPC with guaranteed nominal stability has some ability to deal with disturbances.[40]

3.2 Efficient implementation

In this subsection, an efficient approach is proposed for implementing autonomous drifting in real time, namely Koopman-based MPC, where Koopman operator theory and DMDc are introduced to reduce the computational burden caused by complex nonlinear dynamics. Furthermore, the control problem can be converted to a QP problem.

Koopman operator theory is adopted to construct an alternative discrete-time linear system[25]

$$\varsigma\varphi(\Delta x(k)) = \varphi(\Delta x(k+1) = \varphi(\tilde{f}(\Delta x(k), \Delta u(k))), \tag{25}$$

where ς and φ denote the infinite-dimensional linear operator and the corresponding observation function, respectively.

Since it is difficult to obtain an infinite-dimensional operator in practice, the DMDc algorithm is introduced to approximate ς by finite-dimensional operator,[28] that is, the transformed system (15) is approximately by

$$\Delta x_D(k+1) \approx \mathcal{A}_D \Delta x_D(k) + \mathcal{B}_D \Delta u_D(k), \tag{26}$$

where $\Delta x_D(k) \in \mathbb{R}^3$ and $\Delta u_D(k) \in \mathbb{R}^2$ are the system state and control input, respectively, $\mathcal{A}_D \in \mathbb{R}^{3\times 3}$ and $\mathcal{B}_D \in \mathbb{R}^{3\times 2}$ are matrices that need to be determined from observed data. Define the temporal snapshots of system measurements and control input as data matrices:

$$\mathbf{X_D} = \begin{bmatrix} \Delta x_D^1 & \Delta x_D^2 & \cdots & \Delta x_D^M \end{bmatrix}, \tag{27a}$$

$$\mathbf{X'_D} = \begin{bmatrix} \Delta x_D^2 & \Delta x_D^3 & \cdots & \Delta x_D^{M+1} \end{bmatrix}, \tag{27b}$$

$$\mathbf{U_D} = \begin{bmatrix} \Delta u_D^1 & \Delta u_D^2 & \cdots & \Delta u_D^M \end{bmatrix}, \tag{27c}$$

where $\mathbf{X_D} \in \mathbb{R}^{3\times M}$, $\mathbf{X'_D} \in \mathbb{R}^{3\times M}$, and $\mathbf{U_D} \in \mathbb{R}^{2\times M}$, Δx_D^i and Δu_D^i denote the measurements of Δx_D and Δu_D at time instant i, respectively, M is the number of snapshots. According to (26), the data matrices satisfy

$$\mathbf{X'_D} \approx \mathbf{G_D}\mathbf{\Psi_D} \tag{28}$$

where $\mathbf{G_D} = [\mathcal{A}_D \ \ \mathcal{B}_D]$ and $\mathbf{\Psi_D} = \begin{bmatrix} \mathbf{X_D^T} & \mathbf{U_D^T} \end{bmatrix}^T$.

To find the best-fit solution of operator $\mathbf{G_D}$, singular value decomposition (SVD) is performed on matrix $\mathbf{\Psi_D}$, that is,

$$\mathbf{\Psi_D} \approx \tilde{\mathcal{U}}\tilde{\Sigma}\tilde{\mathcal{V}}^T \tag{29}$$

where the truncation value of SVD is defined as $\tilde{p} = 3$, $\tilde{\mathcal{U}} \in \mathbb{R}^{(3+2)\times 3}$, and $\tilde{\Sigma} \in \mathbb{R}^{3\times 3}$ are unitary and diagonal matrix, respectively.

Then the finite-dimensional approximate matrix is obtained

$$\mathbf{G_D} = [\mathcal{A}_D \ \ \mathcal{B}_D] = \mathbf{X'_D}\tilde{\mathcal{V}}\tilde{\Sigma}^{-1}\tilde{\mathcal{U}}^T, \tag{30}$$

where $\tilde{\mathcal{U}}$ is decomposed as $\tilde{\mathcal{U}} = \begin{bmatrix} \tilde{\mathcal{U}}_1^T & \tilde{\mathcal{U}}_2^T \end{bmatrix}^T$, $\tilde{\mathcal{U}}_1 \in \mathbb{R}^{3\times 3}$, and $\tilde{\mathcal{U}}_2 \in \mathbb{R}^{2\times 3}$. Then matrices $\mathcal{A}_D$ and $\mathcal{B}_D$ can be calculated by:

$$\mathcal{A}_D = \mathbf{X'_D}\tilde{\mathcal{V}}\tilde{\Sigma}^{-1}\tilde{\mathcal{U}}_1^T, \tag{31}$$

$$\mathcal{B}_D = \mathbf{X'_D}\tilde{\mathcal{V}}\tilde{\Sigma}^{-1}\tilde{\mathcal{U}}_2^T. \tag{32}$$

Take the approximately linear model (26) as the prediction model, the problem of stabilizing a vehicle around an unstable equilibrium point can be converted to find a feasible solution to the following optimization problem.

Problem 2.

$$\underset{\Delta\bar{u}_D(\cdot)}{\mathit{minimize}} \quad J_D(\Delta x_D(k), \Delta\bar{u}_D(\cdot)) \tag{33a}$$

$$\text{subject to} \quad \Delta\bar{x}_D(\tau+1|k) = \mathcal{A}_D\Delta\bar{x}_D(\tau|k) + \mathcal{B}_D\Delta\bar{u}_D(\tau|k)), \tag{33b}$$

$$\Delta\bar{x}_D(k|k) = \Delta x_D(k), \tag{33c}$$

$$\Delta\bar{u}_D(\tau|k) \in \Delta U_D, \quad \tau \in [k, k+N-1], \tag{33d}$$

$$\Delta\bar{x}_D(\tau|k) \in \Delta X_D, \quad \tau \in [k, k+N-1], \tag{33e}$$

$$\Delta\bar{x}_D(k+N|k) \in \mathbb{X}_f, \tag{33f}$$

where $\Delta x_D(k)$ is the initial state, $\Delta\bar{x}_D(\tau|k)$ is the predicted state trajectory of system (26), $\Delta\bar{u}_D(\cdot)$ is the control input. The cost function is

$$J(\Delta x_D(k), \Delta\bar{u}_D(\cdot)) = \sum_{i=0}^{N-1} \overline{L}(\Delta\bar{x}_D(k+i|k), \Delta\bar{u}_D(k+i|k)) + \bar{E}(\Delta\bar{x}_D(k+N|k)) \tag{34a}$$

with

$$\overline{L}(\Delta\bar{x}(k+i|k), \Delta\bar{u}_D(k+i|k)) = \Delta\bar{x}_D^{\mathrm{T}}(k+i|k)\overline{Q}\Delta\bar{x}_D(k+i|k) + \Delta\bar{u}_D^{\mathrm{T}}(k+i|k))\overline{R}\Delta\bar{u}_D(k+i|k)), \tag{34b}$$

$$\bar{E}(\Delta\bar{x}_D(k+N|k)) = \Delta\bar{x}_D^{\mathrm{T}}(k+N|k)\overline{P}\Delta\bar{x}_D(k+N|k), \tag{34c}$$

where $\overline{Q} \in \mathbb{R}^{3\times 3}$ and $\overline{R} \in \mathbb{R}^{2\times 2}$ are the positive definite and symmetric weighting matrices.

Since the matrix $[\mathcal{B}_D \quad \mathcal{A}_D\mathcal{B}_D \quad \mathcal{A}_D^2\mathcal{B}_D]$ is full row rank, the symmetric positive-definite matrix $\overline{P}$ of the terminal penalty $\bar{E}(\Delta\bar{x}_D(k+N|k))$ can be solved by (23). The matrix $\Delta u_D = K_D\Delta x_D$ is obtained by LQR such that $A_k = \mathcal{A}_D + \mathcal{B}_D K_D$ is stable, where $Q^* = \overline{Q} + K_D^{\mathrm{T}}\overline{R}K_D \in \mathbb{R}^{3\times 3}$, and $\kappa > 1$ is constant.

To find the terminal set $\mathbb{X}_f$, the maximal admissible set is calculated using algorithm 3.2 proposed by Gilbert and Tan,[42] which satisfies[43,44]

(C3) $\mathbb{X}_f \subseteq \Delta X$, $\mathbb{X}_f$ is closed and $(\mathbf{0}, \mathbf{0}) \in \mathbb{X}_f$,
(C4) $\Delta u_D = K_D\Delta x_D \subseteq \Delta U$, $\forall \Delta x_D \in \mathbb{X}_f$,
(C5) $(\mathcal{A}_D + \mathcal{B}_D K_D)\Delta x_D \in \mathbb{X}_f$.

Accordingly, Problem 2 is converted to a QP problem.

Problem 3.

$$\underset{\overline{\mathbf{U}}(k)}{minimize} \quad \overline{\mathbf{U}}(k)^{\mathrm{T}} H_{QP}\overline{\mathbf{U}}(k) - G_{QP}(k+1|k)^{\mathrm{T}}\overline{\mathbf{U}}(k), \tag{35a}$$

$$\text{subject to} \quad C_{QP}\overline{\mathbf{U}}(k) \geq b_{QP}(k+1|k), \tag{35b}$$

where $\overline{\mathbf{U}}(k) = \left[\Delta\bar{u}_D(k), \Delta\bar{u}_D(k+1), \ldots, \Delta\bar{u}_D(k+N-1)\right]_{N\times 1}^{\mathrm{T}}$ is the manipulated variable. Furthermore, the first element $\Delta\bar{u}_D^*(k)$ of the optimal solution $\overline{\mathbf{U}}^*(k)$ will be applied to the controlled system (11). Due to the space limitation, the derivation of matrices H_{QP}, G_{QP}, C_{QP}, and b_{QP} are omitted.

Remark 3. Two aspects affect the computation time of an optimization problem, that is, optimization method (e.g., Newton method or heuristic search method) and hardware equipment (e.g., FPGA or GPU). In this subsection, the nonlinear model is replaced by an approximately linear model, and the dimensions of the two models are the same. Furthermore, the nonlinear nonconvex optimization problem is converted to a linear convex optimization problem, which improves the computation efficiency. Since the MPC can handle some disturbances and the magnitude of model errors is small, the effect of model errors on the system dynamics can be ignored.

4 | SIMULATION RESULTS

In this section, numerical simulation is carried out to present the effectiveness of the proposed NMPC approach and the efficient implementation for autonomous drifting. Experiments are conducted to demonstrate the superiority of the proposed approach over MPC without guaranteed stability and LQR. The robustness of the proposed approach is illustrated by introducing various model uncertainties. Through the simulation conducted by Koopman-based MPC, the potential of real-time implementing autonomous drifting is shown. The simulation is carried out in Matlab R2015b with Processor Intel® Core™ i7-10700 CPU @ 2.90 GHz and 16.0 GB RAM.

4.1 | Autonomous drifting verification

This subsection presents the effectiveness of the proposed NMPC approach for achieving sustained autonomous drifting. The desired unstable equilibrium point is calculated with $v_x^{ref} = 20$ m/s and $\delta_f^{ref} = -10°$, that is,

$$x^{ref} = \begin{bmatrix} v_y^{ref} & \gamma^{ref} & v_x^{ref} \end{bmatrix}^{\mathrm{T}} = [-5.1 \quad 0.3 \quad 20]^{\mathrm{T}}, \tag{36a}$$

$$u^{ref} = \begin{bmatrix} F_{yf}^{ref} & F_{xr}^{ref} \end{bmatrix}^{\mathrm{T}} = [5879.9 \quad 1970.4]^{\mathrm{T}}, \tag{36b}$$

where (4c) is used to calculate the maximum lateral force of the rear tire.

Then the constraints of the transformed system are calculated by (17):

$$\Delta U = \{\Delta u \in \mathbb{R}^2 \mid -13175.8 \le \Delta F_{yf} \le 1416, \quad -8160.8 \le \Delta F_{xr} \le 4220.0\}, \tag{37a}$$

$$\Delta X = \{\Delta x \in \mathbb{R}^3 \mid -14.9 \le \Delta v_y \le 25.1, \quad -1.3 \le \Delta\gamma \le 0.7, \quad -20 \le \Delta v_x \le 20\}. \tag{37b}$$

Remark 4. Since the form of terminal constraint in (18f) is symmetric, the symmetric constraints are taken for off-line calculation of terminal constraint, that is,

$$\Delta U = \{\Delta u \in \mathbb{R}^2 \mid -1416 \le \Delta F_{yf} \le 1416, \quad -4220.0 \le \Delta F_{xr} \le 4220.0\}, \tag{38a}$$

$$\Delta X = \{\Delta x \in \mathbb{R}^3 \mid -14.9 \le \Delta v_y \le 14.9, \quad -0.7 \le \Delta\gamma \le 0.7, \quad -20 \le \Delta v_x \le 20\}, \tag{38b}$$

which are contained in the sets of (37a) and (37b), and the bounds are taken from the minimum absolute values of the upper and lower bounds of (37a) and (37b).

To calculate the terminal constraint of (18f) and terminal penalty of (19c), the weighting matrices in (19b) are

$$Q = \begin{bmatrix} 250 & 0 & 0 \\ 0 & 250 & 0 \\ 0 & 0 & 30 \end{bmatrix}, \quad R = \begin{bmatrix} 10^{-5} & 0 \\ 0 & 10^{-5} \end{bmatrix}. \tag{39}$$

The linear state feedback control law obtained by LQR is

$$K = \begin{bmatrix} 5639.8 & -30937.5 & 16.4 \\ 420.9 & -325.7 & -1736.0 \end{bmatrix}. \tag{40}$$

Given $\kappa = 1.02$, which satisfies the condition $\kappa > 1$, the terminal penalty matrix is

$$P = \begin{bmatrix} 8566.4 & -24086.8 & -796.1 \\ -24086.8 & 102895.3 & 620.2 \\ -796.1 & 620.2 & 3276.5 \end{bmatrix}, \tag{41}$$

and the constant $\alpha = 13,433$.

As a comparison, an NMPC without guaranteed stability is designed to conduct simulation under the same operating condition, in which the terminal constraint and terminal penalty are not considered. The prediction horizon is $N = 15$.

The initial state is $\Delta x_0 = [-1.2\ \ 0.2\ \ -2]^{\mathrm{T}}$, which corresponds to the initial state $x_0 = [-6.3\ \ 0.5\ \ 18]^{\mathrm{T}}$ of the controlled system (11). The simulation results are shown in Figures 4,5,6,7, and 8, where the solid black lines denote the proposed NMPC approach with guaranteed stability, the blue dash-dot lines represent NMPC without guaranteed stability, the dash red lines are the reference states corresponding to x^{ref}.

As can be seen from the evolution of vehicle states in Figures 4,5, and 6, the proposed NMPC approach can force lateral velocity, yaw rate, and longitudinal velocity quickly converge to the reference values. On the contrary, vehicle states diverge far away from the desired point by NMPC without guaranteed stability. The impact of such considerable state deviations on vehicle lateral stability is intuitively shown in Figures 7 and 8.

As shown in Figure 7, the state trajectories are plotted in v_y - γ phase plane, the black cross denotes the initial point, the pentagrams are the end points, the blue square represents the desired unstable equilibrium point, and the grey shaded area shows the terminal region. Using the proposed NMPC approach, the state trajectory converges to the unstable equilibrium point in the terminal region. Once entering the terminal region, the vehicle states will not leave it, which means that the vehicle states can be stabilized by the proposed approach. However, the NMPC without guaranteed stability can not make the states return to the desired point and diverge in the opposite direction of the terminal region.

The corresponding vehicle positions and postures are shown in Figure 8, where black and blue polygons represent schematic diagrams of the vehicle controlled by NMPC with and without guaranteed stability, respectively, the grey shaded areas are the initial positions, and acute angles denote the vehicle heading direction. It can be seen that vehicle sustained drifting is achieved by the proposed NMPC with guaranteed stability (cf. Figure 8A). However, by NMPC without guaranteed stability, the vehicle seriously skids and gradually turns the heading direction (arrow pointed in Figure 8B), which means that the lateral stability is lost. Such a phenomenon jeopardizes vehicle safety, which is consistent with the disappearance of stability region in subsection 2.2.

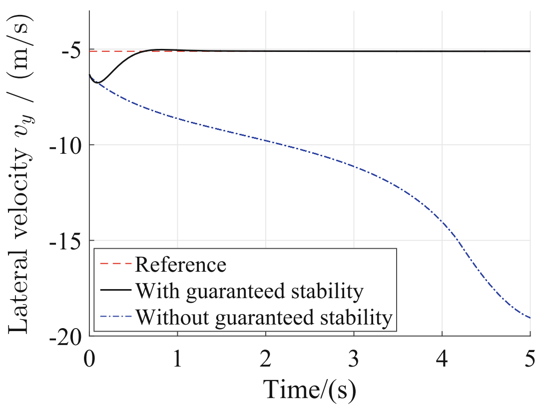

FIGURE 4 The evolution of lateral velocity.

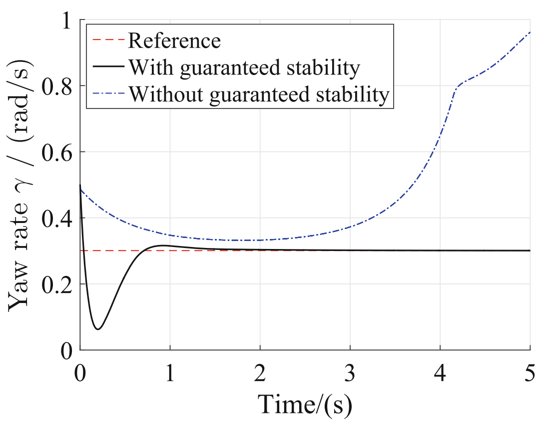

FIGURE 5 The evolution of yaw rate.

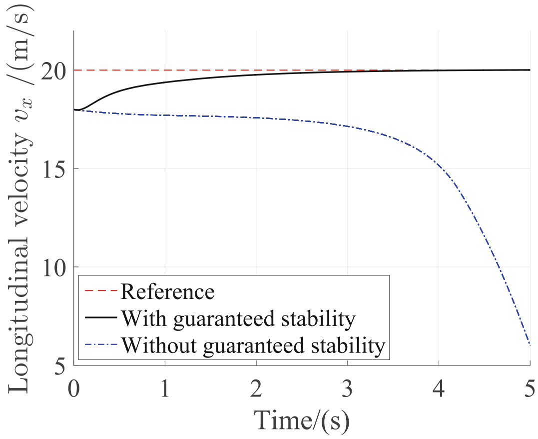

FIGURE 6 The evolution of longitudinal velocity.

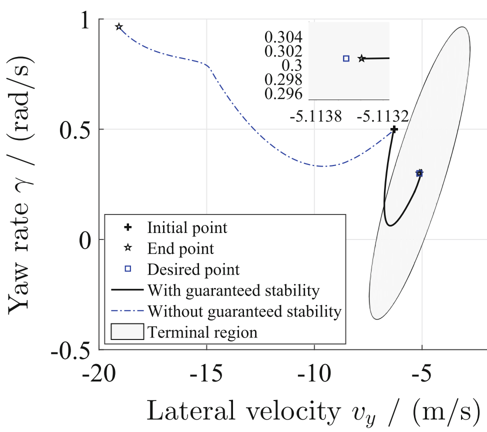

FIGURE 7 States trajectories in $v_y - \gamma$ phase plane.

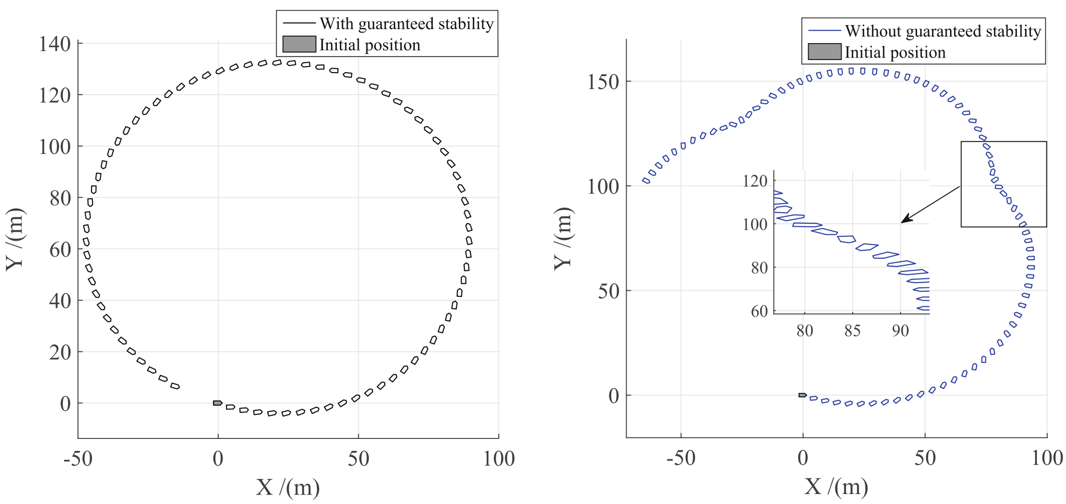

(A) NMPC with guaranteed stability

(B) NMPC without guaranteed stability

FIGURE 8 Vehicle position and posture diagram in inertial coordination.

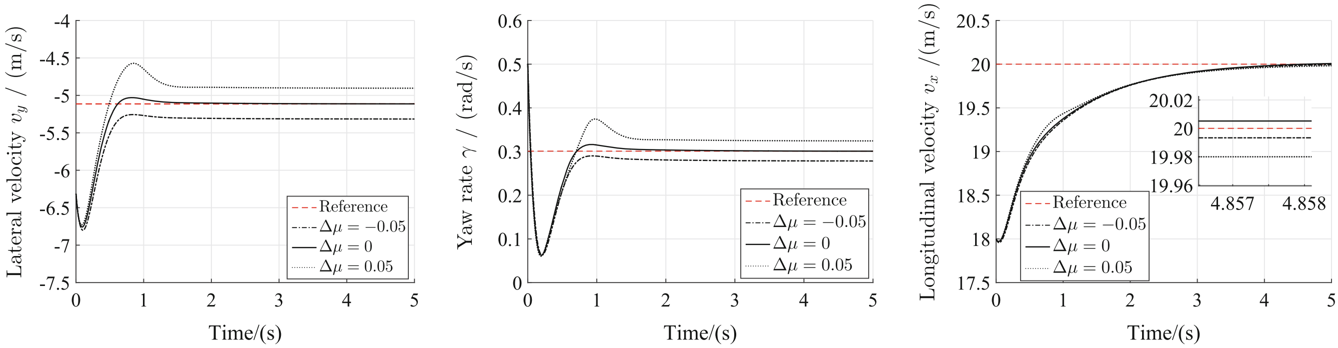

(A) Lateral velocity (B) Yaw rate (C) Longitudinal velocity

FIGURE 9 Uncertainties of road friction coefficient.

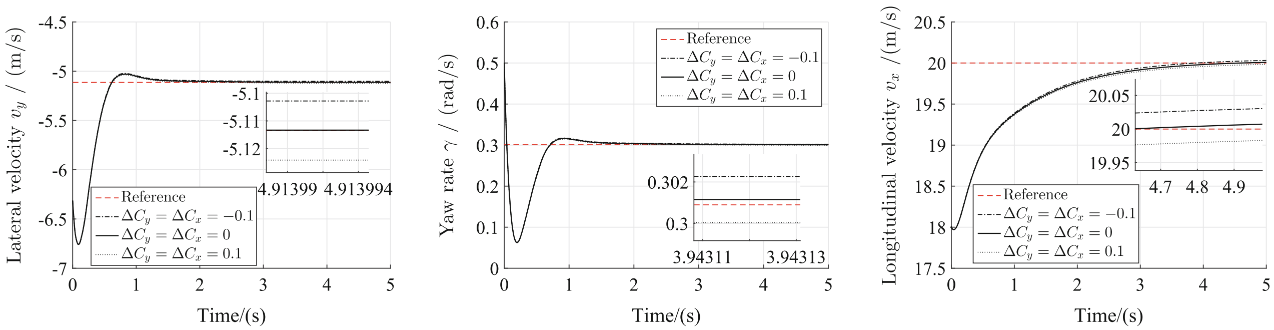

(A) Lateral velocity (B) Yaw rate (C) Longitudinal velocity

FIGURE 10 Uncertainties of air resistance coefficient.

To further illustrate the robustness of NMPC, several uncertainties are considered in the numerical examples. Since changes in driving conditions will affect the vehicle performance in practice, the influence of uncertain road friction coefficient and air resistance coefficient on the system is investigated. The simulation results with $\Delta\mu = \pm 0.05$ deviation from road friction coefficient $\mu = 0.75$ are shown in Figure 9, where solid lines denote $\Delta\mu = 0$, dash-dot lines and dot lines represent $\Delta\mu = -0.05$ and $\Delta\mu = 0.05$, respectively. As seen from Figure 9, the system state can still be stabilized near the reference when the uncertainty of the road friction coefficient exists.

Since the air resistance coefficients C_x and C_y will vary with aerodynamic side slip angle, uncertainties of C_x and C_y are considered. The simulation results of deviations $\Delta C_x = \Delta C_y = \pm 0.1$ ($C_x = 0.37, C_y = -0.35$) are shown in Figure 10, where solid lines denote $\Delta C_x = \Delta C_y = 0$, dash-dot lines and dot lines represent $\Delta C_x = \Delta C_y = -0.1$ and $\Delta C_x = \Delta C_y = 0.1$, respectively. As shown in Figure 10, although uncertainties of air resistance coefficient exist, the system is still stable with the proposed NMPC, and the steady-state error is small. The simulation results show the robustness of NMPC to model uncertainties.

4.2 | Real-time implementation

In this subsection, comparative experiments are conducted to present the effectiveness of Koopman-based MPC.

To obtain the approximately discrete-time linear model (26), the input-output data of the system (15) is collected to construct data matrices (27). The sequence $\mathbf{X}_{\mathbf{D}}'$ is predicted by $\mathbf{X}_{\mathbf{D}}$ and $\mathbf{U}_{\mathbf{D}}$ with the snapshot number $M = 80$. Then 200 trajectories are collected by:

1. initial values of states randomly selected in $v_y \in [-1, 1]$ m/s, $\gamma \in [-0.1, 0.1]$ rad/s, and $v_x \in [-2, 2]$ m/s,
2. control inputs randomly selected in $F_{yf} \in [-200, 200]$ and $F_{xr} \in [-200, 200]$,

where the sets are symmetric because $(\mathbf{0}, \mathbf{0})$ is the desired equilibrium point of the transformed system. The sets are relatively small for better fitting the nonlinear dynamics near unstable equilibrium point.

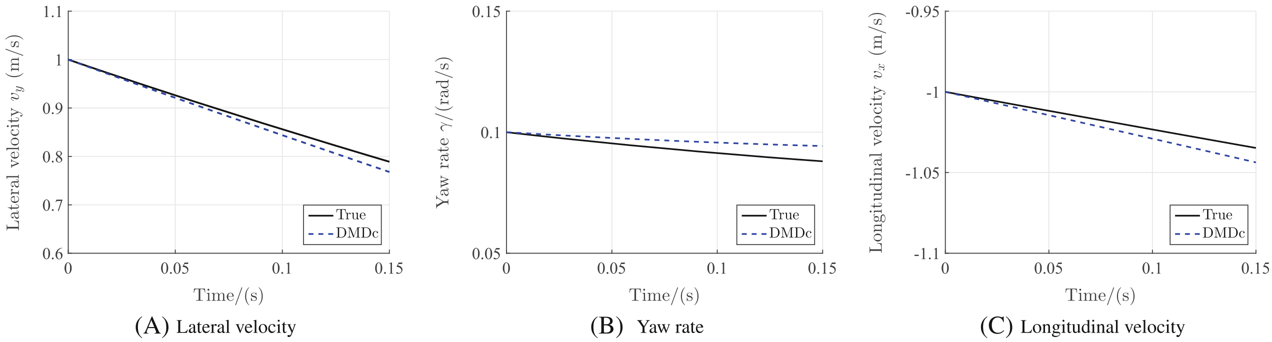

FIGURE 11 Validation of Koopman linear model.

The root mean square error (RMSE) is used to evaluate the deviation between model (26) and (15), that is,

$$\mathrm{RMSE} = \frac{\sqrt{\sum_{k=1}^{N} \|x_{\mathrm{DMDc}}(k) - x_{\mathrm{true}}(k)\|_2^2}}{\sqrt{\sum_{k=1}^{N} \|x_{\mathrm{true}}(k)\|_2^2}} \times 100\%, \tag{42}$$

where $x_{\mathrm{DMDc}}(k)$ and $x_{\mathrm{true}}(k)$ are the states predicted by (26) and (15), respectively. The system evolutions of (15) and (26) are shown in solid black lines and dash blue lines of Figure 11, respectively. The initial state is $x_{\mathrm{DMDc}}(0) = x_{\mathrm{true}}(0) = [1 \;\; 0.1 \;\; -1]^{\mathrm{T}}$, the control input is $u_{\mathrm{DMDc}} = [0 \;\; 0]$, and the predictive horizon is $N = 15$. The RMSE is 0.95%, that is, the deviation is small and the (26) can be used as the prediction model (33b) in Problem 2.

Then, Problem 2 can be solved. To verify the proposed approach, the desired unstable equilibrium point is set with $\delta_f^{ref} = -10°$ and $v_x^{ref} = 30$ m/s, that is,

$$x^{ref} = \begin{bmatrix} v_y^{ref} & \gamma^{ref} & v_x^{ref} \end{bmatrix}^{\mathrm{T}} = [-7.62 \quad 0.20 \quad 30]^{\mathrm{T}}, \tag{43a}$$

$$u^{ref} = \begin{bmatrix} F_{yf}^{ref} & F_{xr}^{ref} \end{bmatrix}^{\mathrm{T}} = [5749.1 \quad 2176.9]^{\mathrm{T}}. \tag{43b}$$

Then the constraints in (33d) and (33e) are obtained from (17):

$$\Delta U_D = \{\Delta u_D \in \mathbb{R}^2 \mid -13045 \le \Delta F_{yf} \le 1546.8, \;\; -8367.3 \le \Delta F_{xr} \le 4013.5\}, \tag{44a}$$

$$\Delta X_D = \{\Delta x_D \in \mathbb{R}^3 \mid -12.38 \le \Delta v_y \le 27.62, \;\; -1.2 \le \Delta\gamma \le 0.8, \;\; -30 \le \Delta v_x \le 10\}. \tag{44b}$$

The weighting matrices in (34b) for calculating the terminal constraint (33f) and terminal penalty (34c) are consistent with (39), that is, $\overline{Q} = Q$ and $\overline{R} = R$. Then linear state feedback control law obtained by LQR is

$$K_D = \begin{bmatrix} 5142.1 & -33979.5 & 106.6 \\ 499.1 & -537.7 & -1748.2 \end{bmatrix}. \tag{45}$$

The weighting matrix of (34c) is

$$\overline{P} = \begin{bmatrix} 6085.7 & -19208.9 & -595.3 \\ -19208.9 & 101430.6 & 86.2 \\ -595.3 & 86.2 & 2990.0 \end{bmatrix}. \tag{46}$$

As a comparison, an MPC without guaranteed stability is designed to conduct simulation under the same operating condition. The prediction horizon is $N = 15$. The initial state is $\Delta x_D(0) = [-1 \;\; 0.2 \;\; -2]^{\mathrm{T}}$, which corresponds to the initial state $\Delta x_0 = [-8.62 \;\; 0.40 \;\; 28]^{\mathrm{T}}$ of the controlled system (11). The simulation results are shown in Figures 12,13,14, and 15, where the solid black lines denote the results of Koopman-based MPC, the blue dash dot lines represent MPC without guaranteed stability, the dash red lines are the reference states corresponding to x^{ref}.

It can be seen from Figures 12,13, and 14 that vehicle lateral velocity, yaw rate, and longitudinal velocity can track the reference states with small deviations. However, an MPC without guaranteed stability can not stabilize vehicle states. State trajectories show such phenomenon in $v_y - \gamma$ phase plane (cf. Figure 15), where the region surrounded by the solid grey lines represents the projection of the terminal region on the $v_y - \gamma$ phase plane, which is composed of multiple linear constraints represented by a polyhedron. Compared with an MPC without guaranteed stability, the proposed approach can force states to the terminal region and to converge to the desired unstable equilibrium point.

Furthermore, simulation results with uncertain road friction coefficients and air resistance coefficients are shown in Figures 16 and 17, respectively, where solid lines represent $\Delta\mu = 0$ ($\mu = 0.75$) and $\Delta C_x = \Delta C_y = 0$ ($C_x = 0.37$ and $C_y = -0.35$), dash dot lines represent $\Delta\mu = -0.05$ and $\Delta C_x = \Delta C_y = -0.1$, and dot lines denote $\Delta\mu = 0.05$ and $\Delta C_x = \Delta C_y = 0.1$. It shows that, the deviations between vehicle states and the reference states are small with the proposed approach, that is, the proposed approach can deal with some model perturbations.

In addition, a more general disturbance is considered in the controlled system (11), that is,

$$x(k+1) = F(x(k), u(k)) + d(k). \tag{47}$$

where

$$d(k) = \begin{cases} [0.01 \quad -0.01 \quad 0.01]^{\mathrm{T}}, & \text{if } 55 \le k \le 65, \\ [0 \quad 0 \quad 0]^{\mathrm{T}}, & \text{if } 0 \le k < 55, 65 < k \le 500. \end{cases}$$

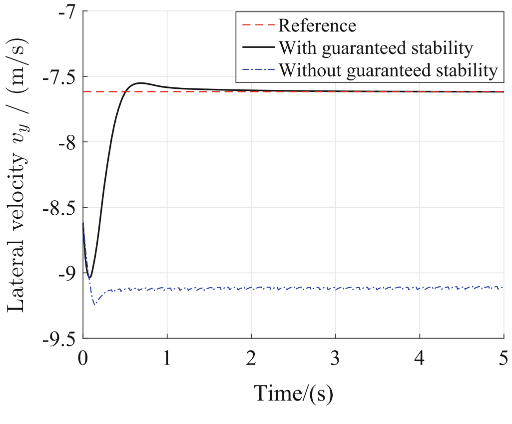

FIGURE 12 The evolution of lateral velocity.

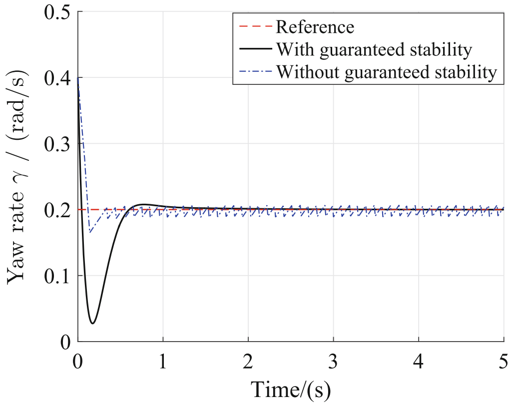

FIGURE 13 The evolution of yaw rate.

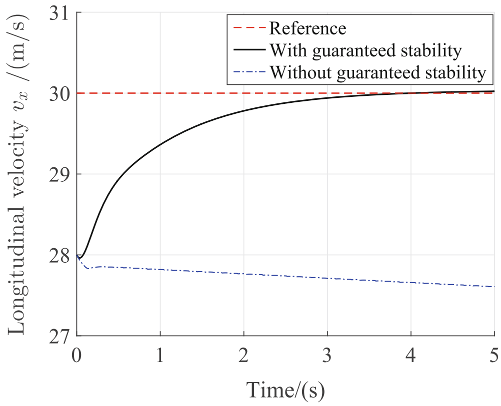

FIGURE 14 The evolution of longitudinal velocity.

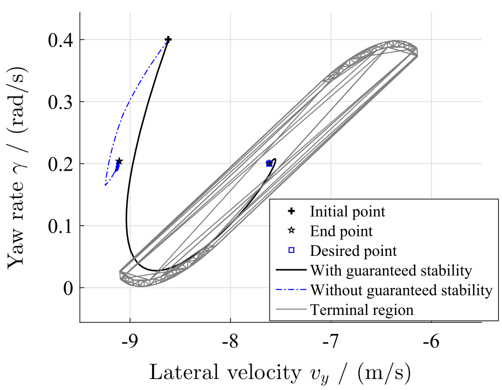

FIGURE 15 States trajectories in $v_y - \gamma$ phase plane.

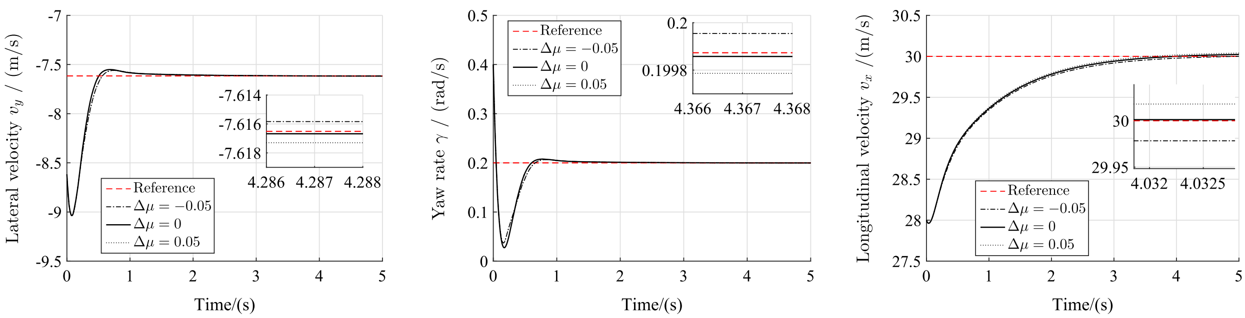

(A) Lateral velocity (B) Yaw rate (C) Longitudinal velocity

FIGURE 16 Koopman-based MPC with uncertainties of road friction coefficient.

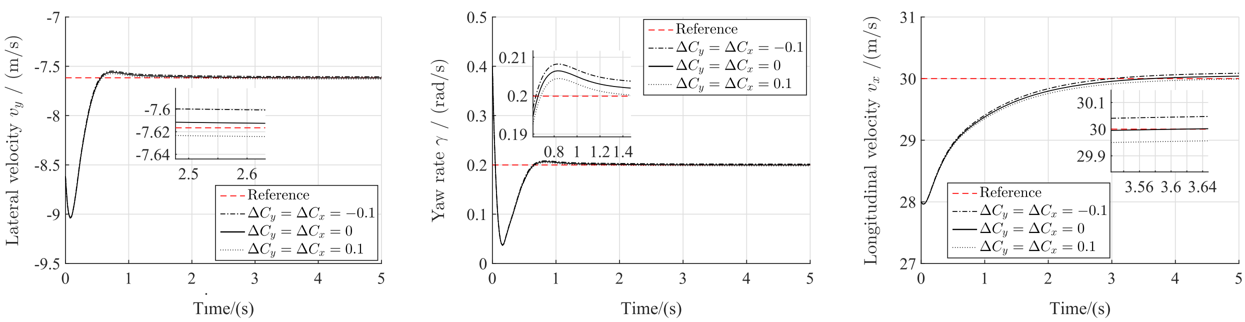

(A) Lateral velocity (B) Yaw rate (C) Longitudinal velocity

FIGURE 17 Koopman-based MPC with uncertainties of air resistance coefficient.

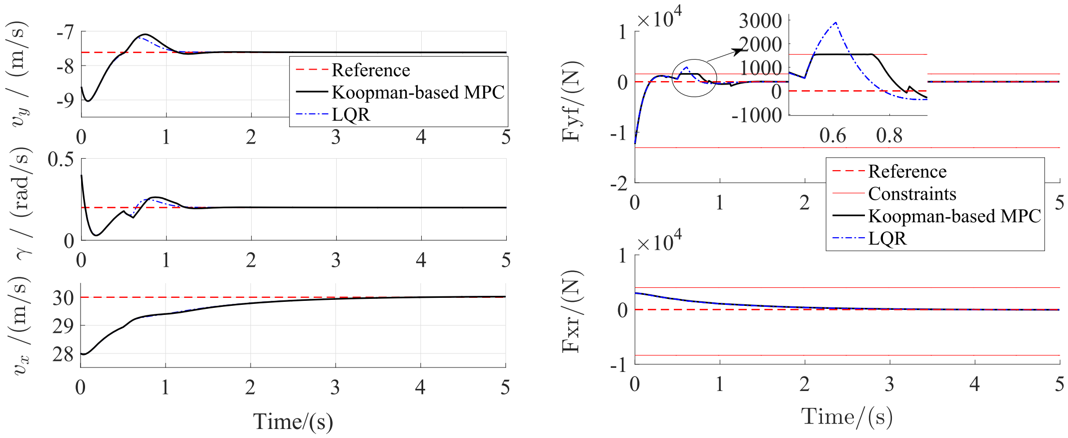

(A) States (B) Control inputs

FIGURE 18 Comparison between Koopman-based MPC and LQR.

The simulation results of the comparison between Koopman-based MPC and LQR are shown in Figure 18. Figure 18A,B are the evolutions of states and control inputs, respectively, in which the solid black lines represent Koopman-based MPC, blue dash dot lines represent LQR, red dot lines denote the references, solid red lines are the constraints of control inputs. As shown in Figure 18, the proposed approach enables the vehicle states to track the reference values while satisfying the control constraints. In contrast, although LQR can drive vehicle states to the reference values, it cannot handle any constraint, cf. Figure 18B.

Note that the average computation time of the NMPC and the Koopman-based MPC are 512 and 4.5 ms, respectively. The computation time of the former is much longer than the sampling time $T_s = 10$ ms. That is, the Koopman-based MPC approach is efficient and promising for implementing vehicle drifting in real time.

5 | CONCLUSIONS

This paper proposed an NMPC approach for autonomous vehicle drifting, in which stability around an unstable equilibrium was guaranteed. Based on the 3-DOF vehicle model with a nonlinear tire model, vehicle dynamics characteristics concerning stability region were analyzed by the phase plane method, and the desired unstable equilibrium point was calculated. An NMPC with guaranteed stability was designed, which forces vehicles in a sustained drift, that is, stability around its single unstable equilibrium. The Koopman operator theory and DMDc algorithm were introduced to obtain the approximately linear model, which reduced the computational burden caused by nonlinear dynamics. Then the control problem was converted to a QP problem that could be solved within a sampling time. The simulation was conducted with various system uncertainties. Compared with MPC without guaranteed stability and LQR, the effectiveness and superiority of the proposed scheme for ensuring vehicle safety under extreme conditions were illustrated. Future work is to design a tube MPC within the framework of Koopman-based MPC.[27]

ACKNOWLEDGMENTS

This work is supported by the National Natural Science Foundation (NNSF) of China under grant nos. (61790564, U1964202, U19A2069), the Natural Science Foundation of Jilin Province (No. YDZJ202101ZYTS169).

CONFLICT OF INTEREST STATEMENT

The authors declare no potential conflict of interests.

DATA AVAILABILITY STATEMENT

The data that support the findings of this study are available from the corresponding author upon reasonable request.

ORCID

Zhuqing Shi https://orcid.org/0000-0002-5110-2782
Shuyou Yu https://orcid.org/0000-0002-3258-6494
Rolf Findeisen https://orcid.org/0000-0002-9112-5946

REFERENCES

1. SAE International. On-road automated vehicle standards committee. *Information Report: Taxonomy and Definitions for Terms Related to On-Road Motor Vehicle Automated Driving Systems*. SAE International; 2014.
2. Wang XB, Shi SM. Analysis of vehicle steering and driving bifurcation characteristics. *Math Prob Eng.* 2015;2015:1-16.
3. Chen WW, Zhang RY, Zhao LF, et al. Control of chaos in vehicle lateral motion using the sliding mode variable structure control. *Proc Inst Mech Eng Part D J Automob Eng.* 2019;233(4):776-789.
4. Liu L, Shi SM, Shen SW, et al. Vehicle planar motion stability study for tires working in extremely nonlinear region. *Chin J Mech Eng Engl Ed*. 2010;23(2):185-194.
5. Liu Z, Payre G. Global bifurcation analysis of a nonlinear road vehicle system. *J Comput Nonlinear Dyn*. 2007;2(4):308-315.
6. Inagaki S, Kushiro I, Yamamoto M. Analysis on vehicle stability in critical cornering using phase-plane method. Paper presented at: AVEC'94, International Symposium on Advanced Vehicle Control, Toyota Motor Corp, Japan. 1994 287-292.
7. Koibuchi K, Yamamoto M, Fukada Y, Inagaki S. *Vehicle Stability Control in Limit Cornering by Active Brake*. SAE Technical Paper. SAE International: 1996.
8. Aga M, Okada A. Analysis of vehicle stability control (VSC)'s effectiveness from accident data. Proceedings: International Technical Conference on the Enhanced Safety of Vehicles, Nagoya, AI. 2003 7.
9. Fennel H, Ding E. *A Model-Based Failsafe System for the Continental TEVES Electronic-Stability-Program (ESP)*. SAE Technical Paper. SAE International: 2000.
10. Joa E, Cha H, Hyun Y, et al. A new control approach for automated drifting in consideration of the driving characteristics of an expert human driver. *Control Eng Pract.* 2000;96:104293.
11. Kolter JZ, Plagemann C, Jackson DT, et al. A probabilistic approach to mixed open-loop and closed-loop control, with application to extreme autonomous driving. Paper presented at: 2010 IEEE International Conference on Robotics and Automation, Anchorage, AK, USA. 2010 839-845.
12. Zhang F, Gonzales J, Li SE, et al. Drift control for cornering maneuver of autonomous vehicles. *Mechatronics*. 2018;54:167-174.
13. Voser C, Hindiyeh RY, Gerdes JC. Analysis and control of high sideslip manoeuvres. *Veh Syst Dyn*. 2010;48:317-336.
14. Hindiyeh RY, Gerdes JC. Equilibrium analysis of drifting vehicles for control design. Paper presented at: ASME Dynamic Systems and Control Conference, Hollywood, California, USA. 2009 48920: 181-188.
15. Park M, Kang Y. Experimental verification of a drift controller for autonomous vehicle tracking: a circular trajectory using LQR method. *Int J Control Autom*. 2021;19(1):404-416.
16. Xu D, Wang G, Qu L, et al. Robust control with uncertain disturbances for vehicle drift motions. *Appl Sci*. 2021;11(11):4917.
17. Hou X, Zhang J, Liu W, et al. *Super-Twisting Second-Order Sliding Mode Control for Automated Drifting of Distributed Electric Vehicles*. SAE Technical Paper, SAE International: 2020.
18. Hindiyeh RY, Christian GJ. A controller framework for autonomous drifting: design, stability, and experimental validation. *J Dyn Syst-T Asme.* 2014;136(5):051015.
19. Velenis E, Katzourakis D, Frazzoli E, et al. Steady-state drifting stabilization of RWD vehicles. *Control Eng Pract.* 2011;19(11):1363-1376.
20. Kuck C. *MPC Design for Autonomous Drifting*. KTH; 2017.
21. Acosta M, Kaarachos S. Teaching a vehicle to autonomously drift: a data-based approach using neural networks. *Knowl-Based Syst.* 2018;153:12-28.
22. Guo HY, Tan ZQ, Liu J, et al. MPC-based steady-state drift control under extreme condition. Paper presented at: 33rd Chinese Control and Decision Conference (CCDC). 2021 4708-4712.
23. Hu C, Zhou X, Duo R, et al. Combined fast control of drifting state and trajectory tracking for autonomous vehicles based on MPC controller. Paper presented at: International Conference on Robotics and Automation (ICRA), IEEE. 2022 1373-1379.
24. Shen J, Hong D. Optimal linearization via quadratic programming. *IEEE Robot Autom Lett.* 2020;5(3):4572-4579.
25. Koopman BO. Hamiltonian systems and transformation in Hilbert space. *Proc Natl Acad Sci USA.* 1931;17:315-318.
26. Korda M, Mezić I. Linear predictors for nonlinear dynamical systems: Koopman operator meets model predictive control. *Automatica*. 2018;93:149-160.
27. Zhang XL, Pan W, Scattolini R, Yu SY, et al. Robust tube-based model predictive control with Koopman operators. *Automatica*. 2022;137:110114.
28. Proctor JL, Brunton SL, Kutz JN. Dynamic mode decomposition with control. *Siam J Appl Dyn Syst.* 2016;15:142-161.
29. Yu SY, Sheng EC, Zhang YJ. Efficient nonlinear model predictive control of automated vehicles. *Mathematics*. 2022;10(21):4163.
30. Masoto A. *Vehicle Handling Dynamics*. Butterworth-Heinemann; 2009.
31. Pacejka B. *Tire and Vehicle Dynamics*. Butterworth-Heinemann; 2012.
32. Peng H, Ozaki T, Haggan-Ozaki V, et al. A parameter optimization method for radial basis function type models. *IEEE Trans Neural Netw*. 2003;14(2):432-438.
33. Khalil HK. *Nonlinear Systems*. Third ed. Patience Hall; 2002.

34. Ono E, Hosoe S, Tuan HD, et al. Bifurcation in vehicle dynamics and robust front wheel steering control. *IEEE Trans Control Syst Technol*. 1998;6(3):412-420.
35. Sadri S, Wu C. Stability analysis of a nonlinear vehicle model in plane motion using the concept of Lyapunov exponents. *Veh Syst Dyn*. 2013;51(6):906-924.
36. True H. On the theory of nonlinear dynamics and its applications in vehicle systems dynamics. *Veh Syst Dyn*. 1999;31(5-6):393-421.
37. Mu Y, Li L, Shi SM. Modified tire-slip-angle model for chaotic vehicle steering motion. *Automot Innov*. 2018;1:177-186.
38. Yu SY, Qu T, Xu F, et al. Stability of finite horizon model predictive control with incremental input constraints. *Automatica*. 2017;79:265-272.
39. Goh JY, Gerdes JC. Simultaneous stabilization and tracking of basic automobile drifting trajectories. Paper presented at: 2016 IEEE Intelligent Vehicles Symposium (IV). 2016 597-602.
40. Yu SY, Reble M, Chen H, et al. Inherent robustness properties of quasi-infinite horizon nonlinear model predictive control. *Automatica*. 2014;50(9):2269-2280.
41. Chen H, Allgöwer F. A quasi-infinite horizon nonlinear model predictive control scheme with guaranteed stability. *Automatica*. 1998;34(10):1205-1217.
42. Gilbert EG, Tan KT. Linear systems with state and control constraints: the theory and application of maximal output admissible sets. *IEEE Trans Automat Contr*. 1991;36(9):1008-1020.
43. Mayne DQ, Rawlings JB, Rao CV, et al. Constrained model predictive control: stability and optimality. *Automatica*. 2000;36(6):789-814.
44. Rawlings JB, Mayne DQ. *Model Predictive Control: Theory and Design*. Nob Hill Publishing; 2009.

How to cite this article: Shi Z, Chen H, Yu S, Findeisen R, Guo H. Nonlinear model predictive control for autonomous vehicle drifting. *Int J Robust Nonlinear Control*. 2023;1-20. doi: 10.1002/rnc.6697